The Astrophysical Journal, 940:107 (8pp), 2022 December 1 https://doi.org/10.3847/1538-4357/ac9d2c

Measurement of High-energy Cosmic-Ray Proton Spectrum from the ISS-CREAM Experiment

G. H. Choi[1], E. S. Seo[2,3], S. Aggarwal[2,3], Y. Amare[2], D. Angelaszek[2,3], D. P. Bowman[3], Y. C. Chen[2,3], M. Copley[2], L. Derome[4], L. Eraud[4], C. Falana[2], A. Gerrety[2], J. H. Han[2], H. G. Huh[2], A. Haque[2,3], Y. S. Hwang[5], H. J. Hyun[5], H. B. Jeon[5], J. A. Jeon[1], S. Jeong[1], S. C. Kang[5], H. J. Kim[5], K. C. Kim[2], M. H. Kim[2], H. Y. Lee[1], J. Lee[5], M. H. Lee[2], L. Lu[2], J. P. Lundquist[2], L. Lutz[2], A. Menchaca-Rocha[6], O. Ofoha[2], H. Park[5], I. H. Park[1], J. M. Park[5], N. Picot-Clemente[2], R. Scrandis[2,3], J. R. Smith[2], R. Takeishi[1], N. Vedenkin[1], P. Walpole[2], R. P. Weinmann[2], H. Wu[2,3], J. Wu[2], Z. Yin[2,3], Y. S. Yoon[2,3], and H. G. Zhang[2]
[1] Department of Physics, Sungkyunkwan University, Republic of Korea; ilpark@skku.edu
[2] Institute for Physical Science and Technology, University of Maryland, College Park, MD, USA; seo@umd.edu, ysy@kriss.re.kr
[3] Department of Physics, University of Maryland, College Park, MD, USA
[4] Laboratoire de Physique Subatomique et de Cosmologie, Grenoble, France
[5] Department of Physics, Kyungpook National University, Republic of Korea
[6] Instituto de Fisica, Universidad Nacional Autónoma de Mexico, Mexico
Received 2022 June 27; revised 2022 October 20; accepted 2022 October 21; published 2022 November 25

Abstract

The Cosmic Ray Energetics And Mass for the International Space Station (ISS-CREAM) experiment successfully recorded data for 539 days from 2017 August to 2019 February. We report the energy spectrum of cosmic-ray protons from the ISS-CREAM experiment at energies from 1.60×10^3 to 6.55×10^5 GeV. The measured spectrum deviates from a single power law. A smoothly broken power-law fit to the data, including statistical and systematic uncertainties, shows the spectral index change at 9.0×10^3 GeV from 2.57 ± 0.03 to 2.82 ± 0.02 with a significance of greater than 3σ. This bump-like structure is consistent with a spectral softening recently reported by the balloon-borne CREAM, DAMPE, and NUCLEON, but ISS-CREAM extends measurements to higher energies.

Unified Astronomy Thesaurus concepts: Galactic cosmic rays (567)

1. Introduction

The cosmic-ray flux decreases rapidly with increasing particle energy. The all-particle spectrum follows a grand power law with spectral features known as the "knee," where the spectrum softens at $\sim 3 \times 10^6$ GeV, and the "ankle," where the spectrum hardens near $\sim 3 \times 10^9$ GeV. These spectral features have been observed through ground-based experiments by measuring air showers from the particles' interactions in the atmosphere for the energy range above $\sim 10^5$ GeV.

Instruments with particle detectors mounted on satellites or balloons, and recently on the International Space Station (ISS) are utilized to measure the cosmic rays before they interact with Earth's atmosphere. They identify the primary particles and determine their energy. These direct measurements provide information on cosmic-ray elemental spectra and their relative abundances of different elements.

However, direct measurements of cosmic rays above $\sim 10^3$ GeV have been challenging because of their instrument size limitations for low cosmic-ray fluxes. The Cosmic Ray Energetics And Mass (CREAM) experiment was developed to extend direct measurements to these energies (from $\sim 10^3$ to $\sim 10^6$ GeV). It was successfully flown on balloons seven times over Antarctica (called CREAM-I to VII) between 2004 and 2016 and accumulated 191 days of flight time. It was then transformed for deployment on the ISS, also known as ISS-CREAM (Seo et al. 2014).

The CREAM-I and II experiments reported a spectral hardening of elemental spectra near 200 GeV nucleon^{-1} (Ahn et al. 2010). It was shown that the proton and helium spectra are harder than the prior lower-energy data and directly measured hardening above $\sim$200 GeV nucleon^{-1} for heavier nuclei. The Payload for Antimatter–Matter Exploration and Light-nuclei Astrophysics (Adriani et al. 2011) later directly measured proton and helium spectra confirming spectral hardening at $\sim$200 GV. It was rather a sharp hardening mainly due to limited statistics. The Alpha Magnetic Spectrometer-02 (AMS-02; Aguilar et al. 2015, 2017, 2020), with better precision, reported progressive spectral hardening of proton, helium, and other heavier elements at the same rigidity. More recently, the DArk Matter Particle Explorer (DAMPE; An et al. 2019) and the Calorimetric Electron Telescope (CALET; Adriani et al. 2019) also reported spectral hardening of protons at similar energies.

CREAM-III (Yoon et al. 2017) reported possible softening at $\sim 2 \times 10^4$ GeV by reaching higher energies than previous experiments. More recently, DAMPE reported spectral softening at 1.36×10^4 GeV (An et al. 2019), confirming the CREAM-III results. NUCLEON (from "nucleon" to nuclear particle) also reported spectral softening at $\sim 10^4$ GeV (Atkin et al. 2018; Grebenyuk et al. 2019). Detailed measurement of the high-energy spectra is of great interest for understanding cosmic-ray origin, acceleration, and propagation. In this Paper, we report the measurement of the proton spectrum for the energy range from 1.60×10^3 to 6.55×10^5 GeV from the ISS-CREAM experiment.

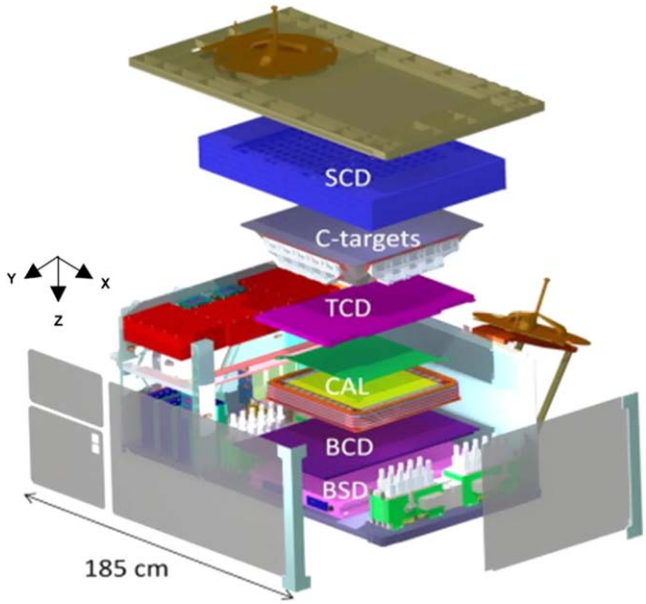

Figure 1. Exploded view of the ISS-CREAM instrument (Seo et al. 2014).

2. ISS-CREAM Experiment

2.1. ISS-CREAM Instrument

The ISS-CREAM instrument was designed to measure protons to iron nuclei in the energy range from $\sim 10^3$ to $\sim 10^6$ GeV. It comprises a silicon charge detector (SCD), carbon targets (C-targets), a calorimeter (CAL), a top counting detector (TCD), a bottom counting detector (BCD), and a boronated scintillator detector (BSD), as illustrated in Figure 1.

The SCD provides the charge measurement of incident cosmic rays for particle identification. The signal from the silicon sensor reflects the ionization energy loss per unit path length (dE/dx) of an incident particle, which is proportional to the square of the incident charge (Z). The SCD is at the top of the ISS-CREAM instrument and consists of four layers. This multilayer configuration can provide redundant charge measurements, which reduce the risks associated with a long operation in space. Each of the four SCD layers covers an active detection area of 78.2 × 73.6 cm. It is finely segmented with 2688 silicon pixels of 1.37 × 1.57 × 0.05 cm each. This fine segmentation minimizes contamination of the backscattered particles from detectors below the SCD in the charge measurements (Park et al. 2007). The SCD module was exposed to the heavy-ion beams of 60 GeV nucleon^{-1} with $A/Z = 2$ nuclear fragments at the European Organization for Nuclear Research (CERN) in 2016 November for a calibration (Lee et al. 2019).

The carbon targets are located just below the SCD. They comprise two high-density ($\rho = 1.92$ g cm^{-3}) 9.5 cm thick graphite blocks with a 30° flare angle cemented in carbon-fiber/epoxy composite. The carbon targets induce hadronic interactions, which generate hadronic showers in the CAL (Ahn et al. 2007).

The CAL provides particle energy measurements utilizing 20 layers of tungsten/scintillating fibers. Each of the 20 layers consists of a 50 cm × 50 cm × 3.5 mm (one radiation length thick) tungsten plate, followed by a layer of 50 1 cm wide 50 cm long scintillating-fiber ribbons (Ahn et al. 2007). Each 1 cm wide ribbon is made of 19 0.5 mm diameter scintillating fibers (BCF-12MC). Ribbons are oriented perpendicular to the ribbons of the neighboring layers. Therefore, the ribbons provide X–Z positions for every other 10 layers, and those in the other alternating 10 layers provide Y–Z positions. The light signal from each ribbon is collected using an acrylic light mixer coupled to a bundle of clear fibers. The clear fiber bundles are connected to hybrid photodiodes (HPDs). Signals are measured by converting the scintillation lights to electrons, amplified by high voltage power supplies in the HPD (Lee et al. 2009).

To calibrate the signals into corresponding energy units, CAL was calibrated in a series of beam tests at CERN, where the highest-energy test beams are available. Its performance was tested with various particle beams (Ahn et al. 2006; Yoon et al. 2007). The beam test data are in good agreement with detailed Monte Carlo (MC) simulations (Zhang et al. 2021 and references therein). The MC simulations show that the calorimeter response is quite linear, and the energy resolution is energy independent over the CREAM measurement range (Wu et al. 2019). The total deposited energy from the sum of all scintillating-fiber ribbons determines cosmic-ray incident energy. To find the direction of cosmic rays, the shower axis of the incident cosmic ray is reconstructed from signals in the CAL ribbons. This reconstructed shower axis is extrapolated to the SCD. The trajectory intersection with the SCD plane allows identification of the incident cosmic rays (Lundquist et al. 2019). The CAL also provides a high-energy trigger.

The TCD and BCD (TCD/BCD) with segmented photodiodes are located above and below the CAL, respectively, to provide additional layers for the longitudinal and lateral shower profiles measured in the CAL. The electromagnetic showers are usually narrower and more easily depleted than hadronic showers in the CAL. Thus, the TCD/BCD can help distinguish electrons and protons using different shower shapes (Kang et al. 2019). Additionally, TCD/BCD provide a low-energy trigger. TCD and BCD each consist of an array of 20 × 20 photodiodes on a plastic scintillator (EJ-200). The scintillator dimensions are 50 × 50 × 0.5 cm for the TCD and 60 × 60 × 1 cm for the BCD, respectively (Hyun et al. 2015).

The BSD is located at the bottom of the instrument. It can provide additional electron/hadron separation by measuring late signals from thermal neutrons. The BSD comprises a boron-loaded plastic scintillator (EJ-254) with six photomultiplier tubes (Hamamatsu R1924A). The dimension of this scintillator is 60 × 60 × 0.38 cm, and it is loaded with 5% elemental boron by weight with a 20% natural ^{10}B abundance (Amare et al. 2019).

2.2. ISS-CREAM Flight

The ISS-CREAM instrument was launched on board a SpaceX Falcon 9 rocket from NASA's Kennedy Space Center to the ISS on 2017 August 14, as part of the 12th Commercial Resupply (CRS-12) mission. It arrived at the ISS in the unpressurized trunk of the Dragon spacecraft. It was extracted from the trunk and installed on the ISS Japanese Experiment Module Exposed Facility (JEM-EF) #2.

The command uplink and data downlink were via the Tracking and Data Relay Satellite System (TDRSS). All data, including science and housekeeping data, were transferred near real-time through TDRSS. The Science Operations Center at the University of Maryland controlled the ISS-CREAM instrument by sending commands and transferring data from

the Science Flight Computer on board ISS-CREAM (Kim et al. 2019a; Seo et al. 2019).

The ISS-CREAM experiment performed its mission successfully for 539 days. At the beginning of the operation, part of the instrument was turned off during the South Atlantic Anomaly (SAA) transit. Various tests were performed to avoid potential radiation damage to the instrument. In addition, the in-flight calibration, such as periodic charge injections, LED flashes, and pedestal runs, were performed during the flight. Excluding the SAA transit test periods and in-flight calibrations, the live-time is estimated as 228 days. On-orbit performance of the ISS-CREAM SCD, CAL, and TCD/BCD were reported in Choi et al. (2019), Takeishi et al. (2019), Kim et al. (2019b), and Kang et al. (2019), respectively.

3. Data Analysis

This analysis follows the previous balloon-borne CREAM data analysis procedure (Yoon et al. 2011, 2017). We used the Geant3 MC simulation tool (Brun et al. 1987) with the FLUKA hadronic interaction model (Fasso et al. 1993) for consistency with previous balloon-borne CREAM experiments. Protons were generated isotropically in the MC simulation, and the same analysis procedure was applied to MC simulation data to reproduce both flight and calibration data. The attenuation effect in the Earth's atmosphere does not need to be considered for ISS-CREAM data analysis because there is no atmospheric overburden for the ISS-CREAM, unlike the balloon-borne CREAM experiments.

The ISS-CREAM instrument has two physics triggers provided by the CAL and TCD/BCD. The CAL provides a high-energy trigger (EHI) that requires each of any six consecutive layers in the CAL to have at least one ribbon with deposited energy above the threshold (Yoon et al. 2017). The EHI logic of ISS-CREAM is the same as the previous balloon-borne CREAM flights, but the threshold was set higher. Another trigger is a low-energy trigger (ELO) provided by the TCD/BCD that requires a signal above the threshold in at least one out of 400 photodiodes in the TCD and at least two out of 400 photodiodes in the BCD (Kang et al. 2019).

3.1. Event Selection

For this analysis, we selected events that satisfied a physics trigger (EHI or ELO) within the geometry passing through the SCD's top layer and BCD at the bottom. The trajectory of each event was determined by reconstructing the shower axis in the CAL. The reconstructed shower axis was extrapolated back to the SCD, and the incident charge was measured by identifying the SCD pixel that intersected with the trajectory.

Noninteracting particles or particles with the first interaction below the CAL's first layer (late interactions) were removed. These events could result in underestimating the deposited energy in the CAL or misidentifying the incident charge due to the large uncertainty of the trajectory reconstruction (Yoon 2010). The deposited energy of the top four layers was compared with the total deposited energy in the CAL. Their ratio was used to remove the late interactions, as was done for the balloon-borne CREAM analysis. The selected events were required to meet the condition given in Equation (1):

$$\log_{10} E_f(\mathrm{MeV}) \geqslant -0.43 \log_{10} E_t(\mathrm{MeV}) + 0.06, \qquad (1)$$

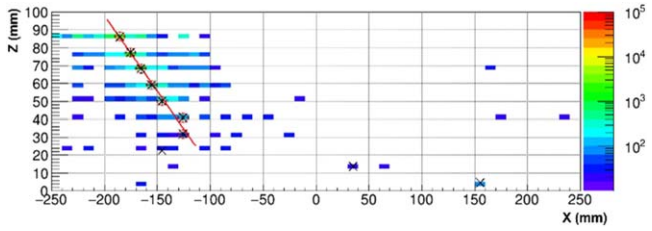

Figure 2. An illustration of the shower axis reconstruction in CAL. The deposited energy in each ribbon is color coded. The largest signal in each layer is marked with an × symbol. The circled cross symbols are included in the final fit (red line).

where E_f is the deposited energy fraction of the top four layers and E_t is the total deposited energy.

3.2. Trajectory Reconstruction

An incident cosmic ray's trajectory is determined by reconstructing its shower axis in the CAL (Ahn et al. 2009; Yoon et al. 2011). For the reconstruction of the shower axis, the first step is to select the ribbon with the largest signal in each layer in the *X*–*Z* and *Y*–*Z* planes of the CAL. The layer with the highest signal and its nearest two layers are selected for a linear fit in both *X*–*Z* and *Y*–*Z* planes. Then, the shower axis of an incident cosmic ray is reconstructed by a chi-squared fit of a straight line through these selected layers.

An initial fit is made for all four combinations of the three selected layers: layers 1 and 2, 2 and 3, 3 and 1, and all three. For each case, by extending this fit to the top and bottom layers of the CAL, the initial-shower axis is reconstructed. The first selection threshold is if the largest signal in each layer is within ±30 mm of *X* (*X*–*Z* plane) and *Y* (*Y*–*Z* plane) from the initial-shower axis (Choi et al. 2021). If the largest signal in the layer is within the ±30 mm area, the layer is selected for the second fit. The second fit with the largest number of layers is chosen as the final fit. The slope of the final fit is compared with four initial fits. It is required for the sign of the final-fit slope to be consistent with at least one out of four initial fits.

Figure 2 illustrates a shower axis reconstruction in the *X*–*Z* plane of an example event; the red line is the final fit using the chosen layers marked with red circles. The ribbons with the largest signal in each layer are marked with × symbols. In this example, the bottom three layers are not included in the final fit because the largest signal in the layer is away from the shower axis (outside ±30 mm area). The trajectory is reconstructed in both the *X*–*Z* and *Y*–*Z* planes of the CAL.

3.3. Charge Determination

To determine a particle's charge, the reconstructed shower axis from the CAL is extrapolated to the SCD. To allow for the tracking uncertainty this introduces, the SCD pixels are scanned for an incident particle within a 3ρ selection area centered on the extrapolated shower axis from the CAL. The use of this selection area size was determined by MC simulations. Among those scanned pixels, the highest-signal pixel is selected to identify an incident particle. The measured signal of the selected pixel is corrected for the particle path length (determined from the reconstructed incidence angle) in the sensor. The SCD signal in an analog-to-digital conversion (ADC) unit is converted to the charge unit using the 2016 CERN beam test results (Lee et al. 2019). In addition, the gain

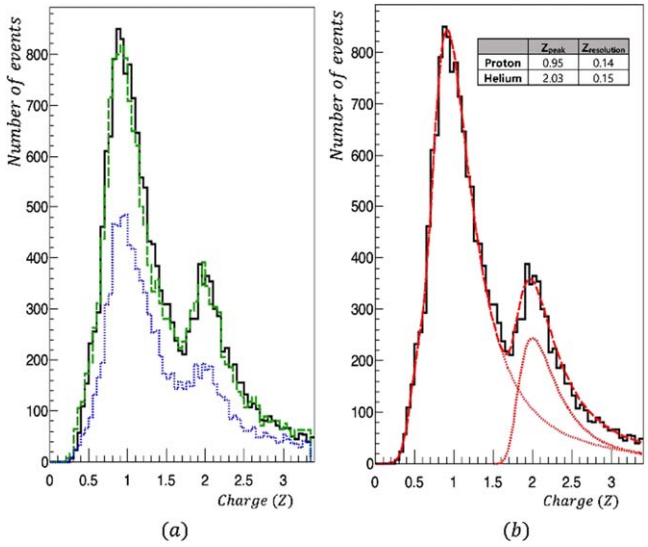

Figure 3. The measured charge distributions of proton and helium nuclei (a) for each layer (black solid line, top layer; green dashed line, second layer; blue dotted line, third layer) and (b) for the top layer with a double Landau-distribution fit (red dashed line). The red dotted lines represent distributions of each component of the proton and helium nuclei for this fit.

corrections for all SCD-electronics channels were performed by the charge injection test for the flight data (Choi et al. 2019).

The measured charge histograms of proton and helium nuclei for the top, second, and third layers of the SCD are shown in Figure 3(a). The statistics of the third layer are lower than the other layers because one quadrant of the third layer was turned off after 2018 August (Choi et al. 2019). The charge peaks and charge resolutions of these three layers are consistent. In this analysis, the top layer of the SCD is used for charge measurements. The data for the top layer of SCD are fitted by a double Landau distribution, and each component of the proton and helium nuclei for this fit is shown in Figure 3(b). The peaks of the proton and helium nuclei are at $Z = 0.95$ and $Z = 2.03$, with corresponding charge resolutions of 0.14 e and 0.15 e, respectively. In this analysis, events are selected in the charge range of $0.7 < Z < 1.7$ for protons following the previous balloon-borne CREAM analysis (Yoon et al. 2011, 2017). The loss of proton events due to the Landau tail is corrected by the charge-selection efficiency, as described in Section 3.5.1.

Backscattered particles are produced from interactions in the detectors below the SCD, particularly carbon targets and the CAL. These particles hit the SCD and disturb the identification of incident cosmic rays. The number of backscattered particles increases as the incident energy of the cosmic rays increases. Based on the proton MC simulations, the charge-misidentification fraction from this effect is estimated to be 3 (±0.05)% at 10^3 GeV and 7 (±0.5)% at the energies of a few 10^4 GeV. At energies above 10^5 GeV, it is 11 (±1.98)% (Wu & Seo et al. 2021).

3.4. Energy Measurement

The CAL and the carbon targets were designed to measure incident cosmic rays' energy. The carbon targets induce hadronic interactions of the incident protons within the geometric acceptance, allowing the CAL to measure deposited energy through the showers (Ahn et al. 2007). The CAL consists of 20 layers of tungsten/scintillating-fiber ribbons.

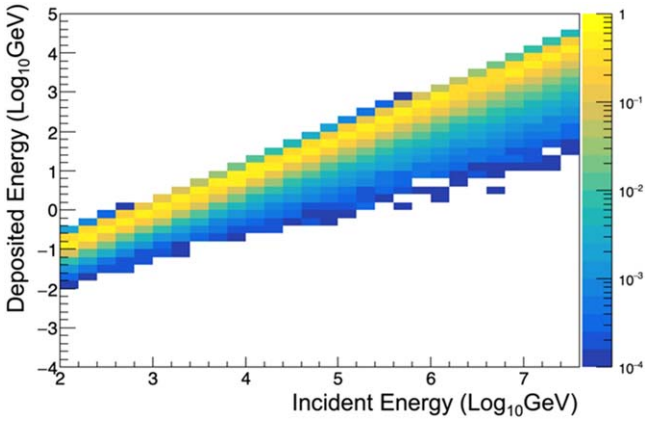

Figure 4. The deconvolution matrix for protons.

Each tungsten plate is followed by a layer of 50 scintillating-fiber ribbons. Each of the 1000 scintillating-fiber ribbons was exposed to 150 GeV electrons by scanning *X*- and *Y*- directions of CAL for calibrations at CERN. The signals of scintillating-fiber ribbons in the ADC unit were converted to the energy unit using the ratio of deposited energy from the MC simulations to the CERN beam test results (Ahn et al. 2006; Han et al. 2011). The calibration factors for the flight data were obtained by taking into account the different HPD settings between the beam test on the ground and the ISS-CREAM flight (Kim et al. 2019b). In addition, the attenuation effects along the scintillating-fiber ribbons were corrected using the analysis result of the beam test (Zhang et al. 2021).

The total deposited energy is measured from the sum of all scintillating-fiber ribbons' deposited energy. The selected protons are counted in each energy bin. The size of the energy bin is determined by the statistical rms resolution of the CAL's energy distributions. Because of the finite energy resolutions, the measured number of events in each energy bin must be corrected for overflows from neighboring bins. This unfolding procedure requires solving a linear equation that converts the measured counts, $N_{\mathrm{dep},j}$, in deposited energy bin *j*to the counts, $N_{\mathrm{inc},i}$, in incident energy bin *i*. The conversion matrix used (Yoon et al. 2011) is given in Equation (2):

$$N_{\mathrm{inc},i} = \sum_j P_{i,j} N_{\mathrm{dep},j}, \tag{2}$$

where the matrix element $P_{i,j}$ is the probability that events in the incident energy bin *i* are from deposited energy bin *j*.

The matrix element $P_{i,j}$ is generated from the proton MC simulation results, as shown in Figure 4. This deconvolution matrix was tested with the input spectrum by changing the power-law index from −2.5 to −2.8. It was confirmed that the flux from the deconvolution process was not sensitive to these assumed indices. The deconvolution matrix was also tested by varying the energy bin size. The energy bin size was determined by considering the energy resolution. Possible uncertainty from varying the energy bin size is included in the error of the spectral index, and it is at the level of 0.004.

3.5. Absolute Flux

The absolute flux F is obtained by correcting the measured proton spectrum for the instrument acceptance, background,

live-time, and efficiencies using Equation (3):

$$F = \frac{dN}{dE}\frac{(1-\delta)}{GF\varepsilon T}, \quad (3)$$

where dN is the number of events in an energy bin, dE is the energy bin size, GF is the geometrical acceptance, $\varepsilon$is the overall efficiency, δ is the charge-misidentified fraction due to backscattered particles, and T is the live-time. The GF is calculated analytically as described in Thomas & Willis (1972). By requiring the incident particle to traverse active areas of the SCD's top layer and BCD at the bottom, the resulting GF is 0.27 ± 0.01 m^2 sr. This result is consistent with GF calculated with MC simulations within the uncertainty. The live-time (T) is estimated to be 228.63 days, excluding the instrument dead-time and the routine periodic calibration time.

3.5.1. Efficiencies

The overall efficiency, ε, contains the efficiencies of all analysis procedures, as shown in Equation (4).

$$\varepsilon = \varepsilon_{\rm trig}\varepsilon_{\rm int}\varepsilon_{\rm rec}\varepsilon_{\rm trac}\varepsilon_{\rm charge}\varepsilon_{\rm SCD_A}. \quad (4)$$

The trigger efficiency, $\varepsilon_{\rm trig}$, is the fraction of triggered events with EHI or ELO among all events within the geometrical acceptance. The interaction efficiency, $\varepsilon_{\rm int}$, is the fraction of events that interacted above the CAL among the triggered events. The trajectory-reconstruction efficiency, $\varepsilon_{\rm rec}$, is the fraction of events in which the reconstructed trajectory passed through the SCD's top layer among the interacted events. The trajectory accuracy efficiency, $\varepsilon_{\rm trac}$, is the fraction of events where the trajectory intersected position is in the SCD's charge-scanning area among all the reconstructed events. The charge-selection efficiency, $\varepsilon_{\rm charge}$, is the fraction of the events within the proton charge range among the selected events.

In addition, the dead or noisy channels are accounted for using the SCD-active-area efficiency, $\varepsilon_{\rm SCDA}$; the ratio of the number of stable channels to the total number of channels in the SCD's top layer. The noisy channels are identified by their large rms pedestal variations throughout the flight. The number of noisy channels varied slightly over time. This noisy-channel variation was taken into account and included in the SCD-active-area efficiency error. The SCD-active-area efficiency is 0.93 ± 0.03.

Efficiencies for the trigger, interaction, trajectory reconstruction, trajectory accuracy, and charge selection are obtained from the MC simulations. The interaction, trajectory reconstruction, and charge selection efficiencies are compared with flight data and found to be consistent. On the other hand, the trigger and trajectory accuracy efficiencies could not be compared with flight data because the measured protons already satisfied the trigger condition, and their actual incident position is unknown in the flight data. The SCD-active-area efficiency is obtained from the flight data. The overall efficiency, ε as a function of the incident energy is shown in Figure 5.

The measured proton fluxes from 1.60×10^3 to 6.55×10^5 GeV are given in Table 1. The statistical uncertainty ($\rho_{\rm stat}$) in each energy bin is estimated using the relation $\delta N_{{\rm ini},i} = \delta(\Sigma_j P_{i,j} N_{{\rm dep},j})$, considering 68.3% of Poisson's confidence interval. The systematic uncertainty ($\rho_{\rm sys}$) is associated with the uncertainties of the overall efficiency (ε), geometric acceptance (GF), live-time (T), and the charge-misidentification fraction (δ). The uncertainty due to the overall efficiency is about 18% at the lowest energy, and it decreases to 3.3% as energy increases. The uncertainty associated with the geometric acceptance is about 3%, and the live-time is about 2%. The uncertainty of the charge misidentification is about 1%. These uncertainties are summed in quadrature to estimate the systematic uncertainty of $\delta_{\rm sys}$. The systematic uncertainty is dominant at low energies, mainly coming from the trigger uncertainty (18% at the lowest energy). However, it gradually decreases as energy increases and ultimately converges to ~5%. Because the showers are developed well in the CAL, the trigger uncertainty improves at high energies. In addition, the uncertainty of the deconvolution procedure is about 0.1% of our obtained spectral indices. It is included in the errors of our obtained spectral indices.

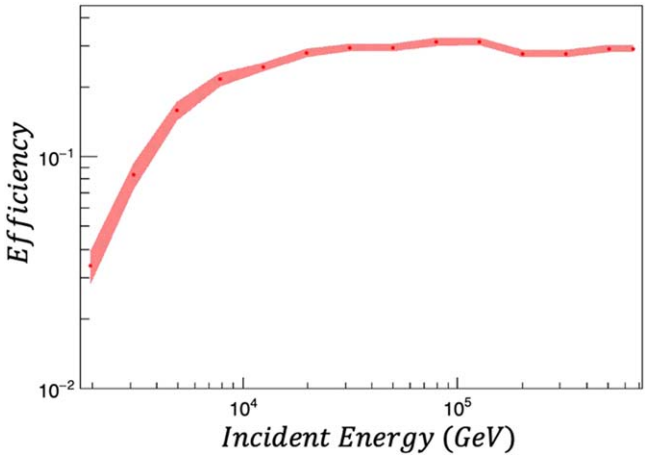

Figure 5. The overall efficiency ε as a function of the incident energy. The shaded area indicates associated uncertainties.

Table 1
ISS-CREAM Proton Fluxes

E_i (GeV)	E_f (GeV)	Flux $\pm \sigma_{\rm stat} \pm \sigma_{\rm sys}$ (m^2 s sr GeV)$^{-1}$
1.60×10^3	2.55×10^3	$(1.24 \pm 0.03^{+0.23}_{-0.15}) \times 10^{-5}$
2.55×10^3	4.04×10^3	$(3.78 \pm 0.08^{+0.52}_{-0.36}) \times 10^{-6}$
4.04×10^3	6.42×10^3	$(1.14 \pm 0.02^{+0.09}_{-0.09}) \times 10^{-6}$
6.42×10^3	1.02×10^4	$(3.51 \pm 0.09^{+0.21}_{-0.23}) \times 10^{-7}$
1.02×10^4	1.62×10^4	$(1.00 \pm 0.04^{+0.05}_{-0.05}) \times 10^{-7}$
1.62×10^4	2.57×10^4	$(2.61 \pm 0.14^{+0.14}_{-0.14}) \times 10^{-8}$
2.57×10^4	4.08×10^4	$(7.10 \pm 0.55^{+0.36}_{-0.39}) \times 10^{-9}$
4.08×10^4	6.48×10^4	$(1.94 \pm 0.23^{+0.10}_{-0.10}) \times 10^{-9}$
6.48×10^4	1.03×10^5	$(5.72 \pm 0.95^{+0.29}_{-0.32}) \times 10^{-10}$
1.03×10^5	1.64×10^5	$(1.40 \pm 0.36^{+0.07}_{-0.08}) \times 10^{-10}$
1.64×10^5	2.60×10^5	$(4.08 \pm 1.64^{+0.20}_{-0.22}) \times 10^{-11}$
2.60×10^5	4.12×10^5	$(1.17 \pm 0.70^{+0.06}_{-0.06}) \times 10^{-11}$
4.12×10^5	6.55×10^5	$(3.88 \pm 3.00^{+0.20}_{-0.21}) \times 10^{-12}$

Figure 6 shows the ISS-CREAM proton spectrum as a function of incident energy together with recent data from other experiments: AMS-02 (Aguilar et al. 2015), CREAM-I+III (Yoon et al. 2017), DAMPE (An et al. 2019), CALET (Adriani et al. 2019), and NUCLEON (Grebenyuk et al. 2019). The fluxes are multiplied by $E^{2.75}$. Our measured proton spectrum is in good agreement with the CREAM-I+III spectrum in the energy range from 1.60×10^3 to 2.60×10^5 GeV, where they

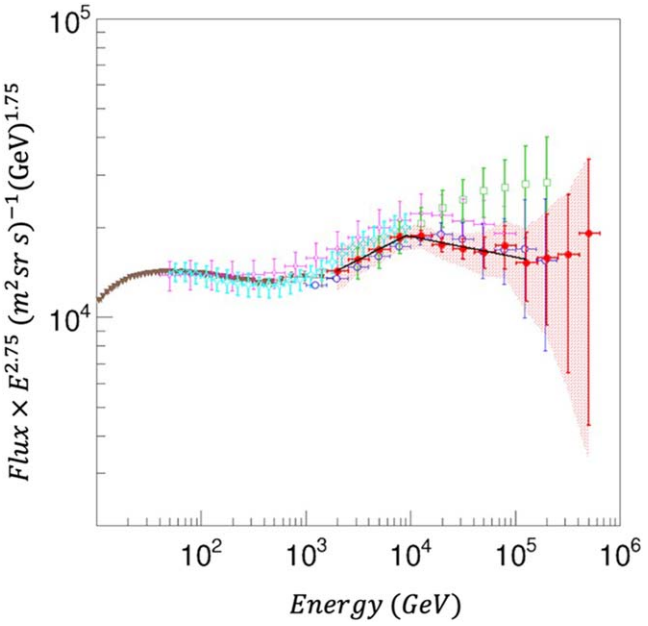

Figure 6. The proton spectrum of the ISS-CREAM experiment (red filled circles) is compared with recent data from other experiments: AMS-02 (brown inverted triangles), combined CREAM-I and III (blue open circles), DAMPE (pink open diamonds), CALET (sky-blue open crosses), and NUCLEON (green open squares). For the ISS-CREAM proton spectrum, the error bars represent statistical uncertainties, and the shaded area is obtained by summing the statistical and systematic uncertainties in quadrature. The black line is the SBPL fit result from the energy range of 1.60×10^3–1.64×10^5 GeV.

overlap. Recently, DAMPE reported the proton spectrum in the energy range from 40 GeV to 10^5 GeV, CALET from 50 to 10^4 GeV, and NUCLEON from 3×10^3 to 2×10^5 GeV. The ISS-CREAM fluxes are slightly lower than both DAMPE and CALET, where they overlap. But, their differences are within 1 $\rho_{\rm tot}$, where $\rho_{\rm tot}$ includes both statistical and systematic uncertainties. Compared to NUCLEON, our fluxes are slightly higher below 10^4 GeV but lower above 10^4 GeV. The difference is within 1 $\rho_{\rm tot}$ and 1.5 $\rho_{\rm tot}$, respectively. NUCLEON fluxes are also higher than DAMPE and prior balloon-borne CREAM-I+III fluxes above 10^4 GeV.

The overall shape of the ISS-CREAM proton spectrum does not follow a single power law. We fit the spectrum with an smoothly broken power law (SBPL) function as given in Equation (5):

$$\Phi = \Phi_0 \left(\frac{E}{E_0}\right)^{-\gamma} \left(1 + \left(\frac{E}{E_b}\right)^{\frac{\Delta\gamma}{\beta}}\right)^{-\beta}, \quad (5)$$

where β is a smooth fit parameter of the transition from the power-law index, γ, below the break energy, E_b, to $\gamma + \Delta\gamma$ above E_b. We tried several SBPL fittings, including statistical and systematic uncertainties, by changing the upper limit of the fit energy range. The fit results for five energy ranges are summarized in Table 2.

The power-law index, γ, is 2.57 for all the fit energy ranges. It changes above the break energy, E_b, by $\Delta\gamma$ of 0.25–0.28, showing the spectrum softening above the break energy. The power-law break energy, E_b, is $(9.6 \pm 0.9) \times 10^3$ GeV for the fit energy range of 1.60×10^3–65×10^3 GeV. It decreases to 8.6×10^3 GeV as the fit energy range increases, but they are within the uncertainties. Our measured spectrum is in better agreement with the SBPL fit, disfavoring a single power-law fit with a significance of 5.7σ for the fit energy range of 1.60×10^3–65×10^3 GeV, 4.2σ for the fit energy range of 1.60×10^3–1.03×10^5 GeV, and 3.1σ for the fit energy range of 1.60×10^3–1.64×10^5 GeV. The significance is less than 3σ for the other two fit ranges with a higher than 1.64×10^5 GeV upper limit of the fit energy range. The SBPL fit result for the energy range of 1.60×10^3–1.64×10^5 GeV is shown with a black line in Figure 6. This bump-like structure due to the spectral index change by $\Delta\gamma$ is consistent with a spectral softening reported by the balloon-borne CREAM, DAMPE, and NUCLEON.

4. Conclusion and Discussion

The measured ISS-CREAM proton spectrum in the energy range of 1.60×10^3–6.55×10^5 GeV is in good agreement with the prior balloon-borne CREAM proton spectra where they overlap, but ISS-CREAM extends measurements to higher energies. A single power law does not represent our spectrum over the whole energy range, so its spectrum is fitted with the SBPL function. Our SBPL fit results for the energy range of 1.60×10^3–1.64×10^5 GeV show that our spectrum softens at the break energy of $(9.0 \pm 1.3) \times 10^3$ GeV. The power-law index is 2.57 ± 0.03 below the break energy and 2.82 ± 0.02 above the break energy. The significance of this fit is 3.1σ, disfavoring a single power-law fit. The significance decreases as the upper limit of the fit energy range increases, indicating the spectral softening does not continue above 1.64×10^5 GeV, but the spectrum becomes harder again. DAMPE reported proton fluxes with an SBPL fit for the energy range of 10^3–10^5 GeV (An et al. 2019). We compare our SBPL fit result for the energy range of 1.60×10^3–1.03×10^5 GeV; the closest to DAMPE's energy range. Our power-law break energy of $(9.0 \pm 1.5) \times 10^3$ GeV is in agreement with DAMPE's break energy of $1.36^{+0.41}_{-0.48} \times 10^4$ GeV within the uncertainty. Both SBPL fit results show the proton spectrum softens above the break energy. The power-law index γ of 2.57 ± 0.04 for ISS-CREAM below the power-law break energy is consistent with DAMPE's power-law index of 2.60 ± 0.01 within the uncertainty. The ISS-CREAM spectral index change $\Delta\gamma$ of 0.25 ± 0.05 is also consistent with DAMPE's $\Delta\gamma$ of 0.25 ± 0.07.

NUCLEON also reported the spectral softening at ~ 10 TV (Atkin et al. 2018; Grebenyuk et al. 2019) with the power-law index change $\Delta\gamma$ of 0.61 (or 0.37), depending on their smoothness fit parameter of $S = 2$ (or $S = \infty$). In comparison with CALET, our power-law index below the break energy is consistent with the CALET's power-law index of 2.56 ± 0.04 for the energy range of 10^3–10^4 GeV (Adriani et al. 2019) within the uncertainty. More recently, CALET reported a preliminary proton spectrum for the energy range of 30–6×10^4 GeV at the ICRC2021 (Kobayashi et al. 2022). Their results show the spectral softening with the break energy of $(1.1 \pm 0.4) \times 10^4$ GeV, which is consistent with our break energy within the uncertainty.

Our ISS-CREAM data are also compared with calculations by Ptuskin et al. (2013), green dotted line; Gaisser et al. (2013), black solid line; Zatsepin & Sokolskaya (2006), blue dashed line in Figure 7. Ptuskin et al. (2013) considered different types of supernova remnants, i.e., type Ia, type IIP, type Ib/c, and type IIb, and their evolution as done for Ptuskin et al. (2010). They further improved their previous calculations to explain

Table 2
SBPL Fit Results for Each Fit Energy Range

Fit Energy Range GeV	γ	E_b GeV	$\gamma + \Delta\gamma$	Significance (σ)
1.60×10^3 –65×10^3	2.57 ± 0.02	(9.6 ± 0.9) × 10^3	2.85 ± 0.02	5.7
1.60×10^3–1.03×10^5	2.57 ± 0.04	(9.0 ± 1.5) × 10^3	2.82 ± 0.02	4.2
1.60×10^3–1.64×10^5	2.57 ± 0.03	(9.0 ± 1.3) × 10^3	2.82 ± 0.02	3.1
1.60×10^3–2.60×10^5	2.57 ± 0.03	(9.0 ± 1.2) × 10^3	2.82 ± 0.02	2.4
1.60×10^3 –6.55×10^5	2.57 ± 0.03	(8.6 ± 1.2) × 10^3	2.82 ± 0.02	2.0

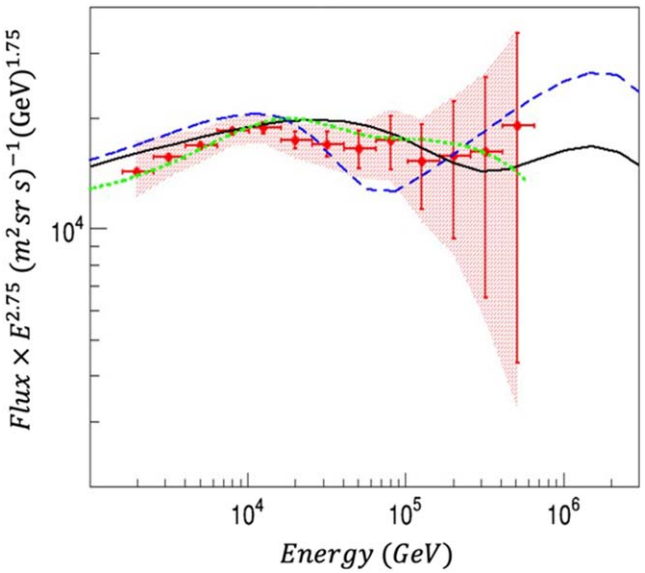

Figure 7. The ISS-CREAM proton spectrum is compared with calculations by Zatsepin & Sokolskaya (2006), blue dashed line; Gaisser et al. (2013), black solid line; Ptuskin et al. (2013), green dotted line.

the spectral hardening around 200 GV and the increased He/p ratio in the energy range of 10^2–10^4 GV. It is assumed that protons are accelerated by the forward shocks in the interstellar medium and by reverse shocks in type II supernova remnants, whereas He and $A/Z = 2$ nuclei are accelerated by the reverse shocks in type I supernova remnants. They calculated steady-state cosmic-ray spectra taking into account magnetic-field amplification and Alfvén drift both upstream and downstream of the shocks. The type IIP supernova remnants accelerate cosmic rays by the forward shocks up to $\sim 10^5$ GeV, and the type Ia and type Ib/c accelerate the cosmic rays up to near the "knee." The reverse shocks in the material of the supernova remnants produce an additional component of cosmic rays resulting in a bump-like structure with a peak near 10^4 GeV.

Gaisser et al. (2013) described the all-particle flux of cosmic rays, including "knee" and "ankle" structures in the energy range of 2×10^2–10^{11} GeV, by considering three populations (populations 1, 2, and 3) of cosmic rays. Each of the three populations has a specific power-law spectral index and rigidity-dependent acceleration limit: $E_{\max\_z} = Z \times E_{\max\_p}$, where Z is the charge, $E_{\max\_z}$ is the acceleration limit of the charged Z particle, and $E_{\max\_p}$ is the acceleration limit for protons. In their calculation, the population 1 flux is calculated using the balloon-borne CREAM-II data to reflect the discrepant hardening above ~200 GV. The cutoff rigidity for population 1 is 120 TV, and cutoff rigidities for populations 2 and 3 are 4 PV and 1.3 EV, respectively. The combination of these three populations is proposed to explain the observed elemental spectra and all-particle spectrum of cosmic rays. In their combination, the population 1 flux is dominant above 200 GV to below the "knee." The population 2 flux is dominant above the "knee" to $\sim 10^9$ GeV, and the population 3 flux is dominant above $\sim 10^9$ GeV.

Zatsepin & Sokolskaya (2006) suggested a mixture of fluxes from three different classes of sources to explain the cosmic-ray spectra in the energy range of 10–10^8 GeV. These three different classes generate rigidity power-law spectra with specific indices and maximum rigidities. For the first source class, nova stars are suggested to accelerate the cosmic rays for a maximum rigidity of 2×10^2 GV. At high energies, the explosion of isolated stars having 8–15 solar masses into the interstellar medium is suggested as the second source class. Cosmic rays from the second source class are accelerated with a maximum rigidity of 5×10^4 GV. Massive stars with 15–25 solar masses exploding (supernovae) into their own stellar wind, known as red supergiants, are suggested as the third source class. Sources of the third class accelerate cosmic rays up the "knee" region to the maximum rigidity of 4×10^6 GV.

Our spectral softening above ~9 TV, as well as previously reported hardening above ~200 GV, contradicts the traditional view that a simple power law can represent cosmic rays without deviations below the "knee." They should be incorporated into a coherent model for the origin, acceleration mechanism, and propagation of cosmic rays. The ISS-CREAM data are being analyzed to check if the same spectral features exist for the $Z \geqslant 2$ nuclei.

This work was supported in the U.S. by NASA grant NNX17AB41G, in Korea by National Research Foundation grants 2021R1A2B5B03002645, 2017K1A4A3015188, 2019H1D3A2A02060090, 2018R1A6A1A06024970, and their predecessor grants, in France by IN2P3/CNRS and CNES, and in Mexico by DGAPA-UNAM project IN109617. The authors thank NASA GSFC WFF and its contractors for engineering support and project management, the JSC ISS Program Office for launch support and ISS accommodation, MSFC for the operational support, and KSC and SpaceX for the launch support. This work was also supported by the MIST (Ministry of Science, ICT), Korea, under the High-Potential Individuals Global Training Program (2021-0-01544) supervised by the IITP (Institute for Information & Communications Technology Planning & Evaluation).

ORCID iDs

L. Lu https://orcid.org/0000-0003-4769-3273
I. H. Park https://orcid.org/0000-0001-6665-9631

References

Adriani, O., Barbarino, G. C., Bazilevskaya, G. A., et al. 2011, Sci, 332, 69
Adriani, O., Akaike, Y., Asano, K., et al. 2019, PhRvL, 122, 181102
Aguilar, M., Aisa, D., Alpat, B., et al. 2015, PhRvL, 114, 171103

Aguilar, M., Ali Cavasonza, L., Ambrosi, G., et al. 2020, PhRvL, 124, 211102
Aguilar, M., Ali Cavasonza, L., Alpat, B., et al. 2017, PhRvL, 117, 251101
Ahn, H. S., Bagliesi, M. G., Beatty, J. J., et al. 2006, NuPhB, 150, 272
Ahn, H. S., Allison, P., Bagliesi, M. G., et al. 2007, NIMPA, 579, 1034
Ahn, H. S., Allison, P., Bagliesi, M. G., et al. 2009, ApJ, 707, 593
Ahn, H. S., Allison, P., Bagliesi, M. G., et al. 2010, ApJL, 714, L89
Amare, Y., Anderson, T., Angelaszek, D., et al. 2019, NIMPA, 943, 162413
An, Hua, Kumamoto, Akihito, Xiang, Rong, et al. 2019, SciA, 5, eaat9459
Atkin, E., Bulatov, V., Dorokhov, V., et al. 2018, JETPL, 108, 5
Brun, R., Bruyant, F., Maire, M., McPherson, A. C., & Zanarini, P. 1987, GEANT 3: User's Guide Geant 3.10, Geant 3.11, CERN-DD-EE-84-01 (Geneva: CERN)https://cds.cern.ch/record/1119728
Choi, G. H., Amare, Y., Angelaszek, D., et al. 2019, ICRC (Madison, WI), 36, 48
Choi, G. H., Aggarwal, S., Amare, Y., et al. 2021, ICRC (Berlin), 37, 94
Fasso, A., Ferrari, A., Ranft, J., & Sala, P. R. 1993, in Proc. 4th Int. Conf. on Calorimetry in High Energy Physics, ed. A. Menzione & A. Scribano (Singapore: World Sci.), 493
Gaisser, T. K., Stanev, T., & Tilav, S. 2013, FrPhy, 8, 748
Grebenyuk, V., Karmanov, D., Kovalev, I., et al. 2019, AdSpR, 64, 2546
Han, J. H., Ahn, H. S., Amare, Y., et al. 2011, ICRC (Beijing), 6, 399
Hyun, H. J., Anderson, T., Angelaszek, D., et al. 2015, NIMPA, 787, 134
Kang, S. C., Amare, Y., Anderson, T., et al. 2019, AdSpR, 64, 2564
Kim, K. C., Amare, Y., Anthony, N., et al. 2019a, ICRC (Madison, WI), 36, 87
Kim, K. C., Amare, Y., Angelaszek, D., et al. 2019b, ICRC (Madison, WI), 36, 88
Kobayashi, K., Marrocchesi, P. S., Adriani, O., et al. 2022, ICRC (Berlin), 37, 98
Lee, J., Amare, Y., Anderson, T., et al. 2019, APh, 112, 8
Lee, M. H., Ahn, H. S., Ganel, O., et al. 2009, IEEE, 56, 1396
Lundquist, J. P., Amare, Y., Angelaszek, D., et al. 2019, ICRC (Madison, WI), 36, 99
Park, I. H., Park, N. H., Nam, S. W., et al. 2007, NIMPA, 570, 286
Ptuskin, Vladimir, Zirakashvili, Vladimir, & Seo, Eun-Suk 2010, ApJ, 718, 31
Ptuskin, Vladimir, Zirakashvili, Vladimir, & Seo, Eun-Suk 2013, ApJ, 763, 47
Seo, E. S., Anderson, T., Angelaszek, D., et al. 2014, AdSpR, 53, 1451
Seo, E. S., Amare, Y., Angelaszek, D., et al. 2019, ICRC (Madison, WI), 36, 137
Takeishi, R., Amare, Y., Angelaszek, D., et al. 2019, ICRC (Madison, WI), 36, 140
Thomas, G. R., & Willis, D. M. 1972, MeScT, 5, 260
Wu, J., Seo, E. S., Aggarwal, S., et al. 2021, ICRC (Berlin), 37, 56
Wu, J., Amare, Y., Angelaszek, D., et al. 2019, ICRC (Madison, WI), 36, 154
Yoon, Y. S. 2010, PhD thesis, Univ. Maryland
Yoon, Y. S., Ahn, H. S., Allison, P. S., et al. 2011, ApJ, 728, 122
Yoon, Y. S., Anderson, T., Barrau, A., et al. 2017, ApJ, 839, 5
Yoon, Y. S., Ahn, H. S., Bagliesi, M. G., et al. 2007, ICRC (Merida), 2, 421
Zatsepin, V. I., & Sokolskaya, N. V. 2006, A&A, 458, 1
Zhang, H. G., Angelaszek, D., Copley, M., et al. 2021, APh, 130, 102583